



From wustite to hematite: thermal transformation of differently sized iron oxide nanoparticles in air

Aladin Ullrich · Niklas Rölle · Siegfried Horn

Received: 25 February 2019 / Accepted: 11 July 2019 / Published online: 28 July 2019
© Springer Nature B.V. 2019

Abstract We have investigated the oxidation behavior of iron oxide nanoparticles in air at elevated temperatures. By wet chemical synthesis under reducing conditions, polycrystalline iron oxide nanoparticles of different sizes were produced. The samples were characterized by x-ray diffraction and transmission electron microscopy. The freshly prepared particles show dominantly the wustite phase and, in addition, one or both of the spinel-like phases maghemite or magnetite. The hematite phase is absent. By annealing under air at different temperatures, we observe a successive transformation of the initial phases to phases of higher oxidation state, until the samples consist completely of the hematite phase. During this transformation, the relative amount and the evolution of the crystallite sizes of the different phases are in the focus of the investigation. We found that the maximum temperature required for a full conversion into the hematite phase depends on the particle size and increases for the larger particles. At the same time, the average crystallite size of the large particles decreases during the initial annealing procedure,

passing through a minimum, before increasing again until single crystalline particles are formed.

Keywords Nanoparticle · Iron oxide · Hematite · Wustite · Magnetite · Maghemite · Phase transformation · High temperatures

Introduction

Transition metal oxide nanoparticles show interesting size-dependent properties due to a wide diversity in their crystal structures and metal oxidation states. For example, iron oxide particles show antiferromagnetic and ferri- or ferromagnetic properties, depending on the oxidation state and crystallographic phase. Iron oxide can crystallize in the halite-, spinel-, and the corundum structures. Magnetic properties of such nanoparticles do not only depend on the oxidation state or crystal structure but are also influenced by finite size effects, resulting, e.g., in superparamagnetism (Bean and Livingston 1959; Berkowitz et al. 1968; Janzen et al. 2003). They also can show enhanced catalytic properties compared with macroscopic material (Li et al. 2003). Therefore, there is a high potential for applications in a variety of fields like catalysis (Liang et al. 2008; Huang et al. 2012; Li et al. 2008), energy storage (Poizot et al. 2000), water treatment (Yavuz et al. 2010), or usage of the magnetic properties in medicine, e.g., as contrast agents or for hyperthermia applications (Fang and Zhang 2009; Armijo et al. 2012; Dutz and Hergt 2013).

A. Ullrich (✉) · N. Rölle · S. Horn
Institute of Physics, University of Augsburg, Universitätsstrasse 1,
86159 Augsburg, Germany
e-mail: aladin.ullrich@physik.uni-augsburg.de

N. Rölle
e-mail: niklasroelle@yahoo.de

S. Horn
e-mail: horn@physik.uni-augsburg.de

The stable crystallographic phase depends, for example, on the oxidation state, crystallite size, and thermodynamic parameters like pressure and temperature. Therefore, various applications require knowledge of the behavior of the particles (e.g., phase transitions) as a function of temperature under ambient atmosphere. From the bulk phase, it is known that under ambient conditions hematite (α -Fe₂O₃) is the most stable phase, while wustite (Fe_{1-x}O) decomposes into metallic iron and magnetite (Fe₃O₄) (Cornell and Schwertmann 2003). The metastable magnetite contains Fe²⁺, which will further oxidize even under ambient conditions to Fe³⁺, resulting in maghemite (γ -Fe₂O₃). Maghemite transforms ultimately at temperatures > 300 °C to the hematite phase (Cornell and Schwertmann 2003; Mendili et al. 2012). In contrast, nanocrystalline maghemite may be stable even for temperatures up to 670 °K (Krispin et al. 2012).

Here we investigate the synthesis of iron oxide nanoparticles and their evolution when treated at elevated temperatures in air.

Experimental section

Particle samples of two different size distributions (40 ± 10 nm, 95 ± 15 nm) were synthesized by thermal decomposition of iron oleate precursor in a high boiling solvent, adapting the procedure described by Park et al. (2004). An iron(III)-oleate complex was used as precursor, synthesized from iron(III)-chloride, oleic acid, and NaOH by wet chemical reaction in a water/ethanol/hexane mixture at 70 °C for 5 h, followed by a subsequent cleaning and drying process, resulting in a dark brown, highly viscous liquid.

The precursor (1 g) was decomposed in pure oleic acid (10 g), acting as high-boiling solvent and reducing agent (Chen et al. 2010) at the same time. The educts were placed in a 250 ml three-neck flask inside a heating mantle. A reflux unit, a thermometer, and a N₂ inlet were attached to the flask.

Two samples were prepared. The first was heated to a temperature of 350 °C within 60 min, the second to 360 °C within 65 min. This resulted in two batches of differently sized and shaped particles, as shown by transmission electron microscopy (TEM), in Figs. 1 a and b, respectively.

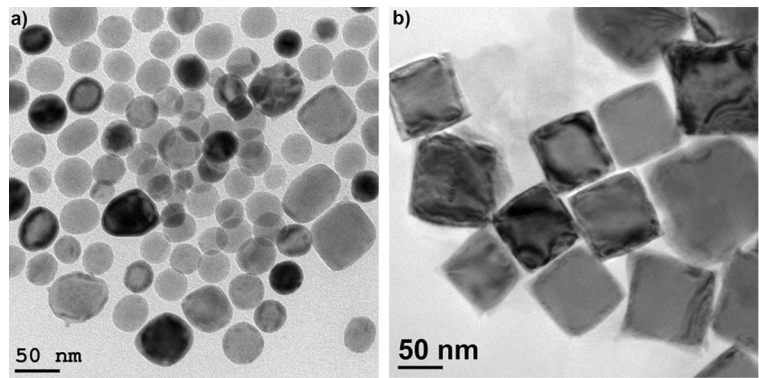
The two batches with different particle sizes are referred to as sample A and B, respectively. Sample A ($T_{\max} = 350$ °C) consists of smaller particles with a

diameter of 40 ± 10 nm and of nearly spherical shape without sharp edges. Sample B ($T_{\max} = 360$ °C) is composed of cubic-like larger particles with an edge length of 95 ± 15 nm. This results in a volume difference between the two kinds of particles of a factor of more than 20. We assume that the different shape can be explained by the difference in total surface area of the particles in the system. Shape control is possible by surfactants like sodium oleate (Kovalenko et al. 2007, Wetterskog et al. 2014, Shavel and Liz-Marzán 2009). During the synthesis, traces of sodium in the precursor may form sodium oleate with the oleic acid. In case of the small particles, few of the particles appear almost cubic, but the sodium oleate concentration is too low to rule the shape of all particles. In case of the larger particles, the total surface area is less, therefore a lower concentration of surfactant is sufficient to cover the surface and alter the particle shape.

After preparation, particles were cleaned three times using the following procedure: 1 ml of the oleic acid-particle-dispersion was diluted with 1–2 ml n-hexane. Then the particles were precipitated with isopropanol, and the dispersion was centrifuged at 6000 rpm for 10 min. After decanting the clear liquid phase that contains side products, the particles were re-dispersed by adding of 2–3 ml n-hexane, and again precipitated with isopropanol. After the last cleaning step, the particles were dispersed in n-hexane and stored in a glass vial. The prepared dispersions were stable, i.e., no precipitation was observed during the experiments. For TEM analysis, particles were deposited on a carbon coated copper grid by dipping the grid into the solution for 1 s, and drying the grid under ambient conditions for several minutes.

For further processing (annealing) and x-ray diffraction (XRD) investigation, the particles were deposited on flat, 25-mm diameter glass substrates. This was performed by applying droplets of the dispersion on the substrate, giving the solvent time to evaporate before applying the next droplet. By this method, several substrates with thick layers (compared to particle size) of particles were produced. These layers were successively annealed at different temperatures for specific time periods (1, 5, 24 h) under ambient conditions and then analyzed by XRD. For temperatures up to 490 °C, a heating plate was used. For higher temperatures, a tube furnace was used. For each annealing temperature, a separate substrate was prepared and used.

Fig. 1 **a** Sample A synthesized at $T_{max} = 350\text{ }^{\circ}\text{C}$. Size range of particles is 30–50 nm; **b** sample B synthesized at $T_{max} = 360\text{ }^{\circ}\text{C}$. Edge length of cubes is 80–110 nm



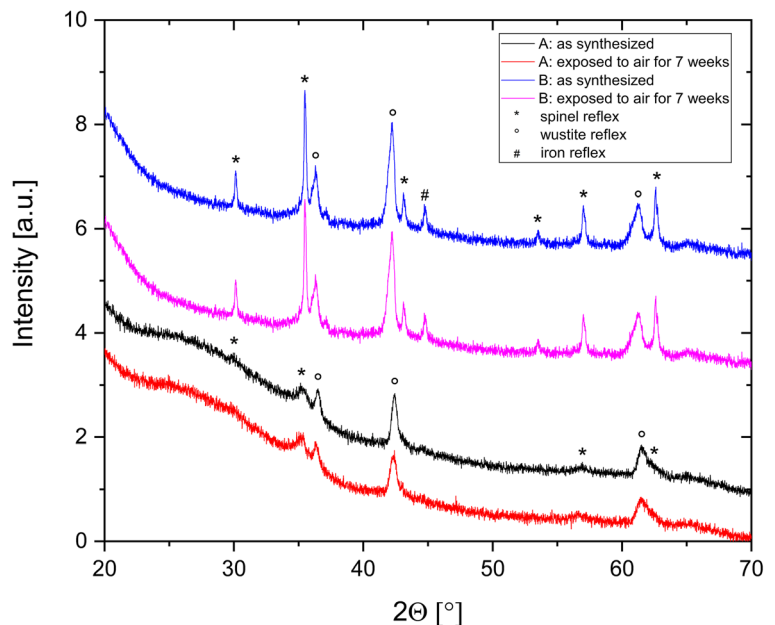
The XRD measurements were performed using copper $K\alpha_1$ and $K\alpha_2$ radiation of a Seifert 3003TT XRD instrument in Bragg-Brentano geometry. The internal peak broadening of the diffractometer was determined by a silicon standard sample. During measurement, the sample was rotated with $\sim 1\text{ Hz}$ for better counting statistics. Data were processed and evaluated with Match! software.

Results I: synthesis

Typical XRD pattern obtained from freshly prepared particles of both types are shown in Fig. 2. All observed reflexes can be assigned to pure iron and iron oxide phases, respectively. The most intense peaks characterize the wustite phase. The other peaks are assigned to

maghemite ($\gamma\text{-Fe}_2\text{O}_3$) or magnetite (Fe_3O_4). These two phases exhibit very similar diffraction pattern except two additional, but weak reflexes for maghemite at 2θ values of 24° and 26° . Therefore, due to peak broadening, resulting from the nanocrystalline nature of the particles, it is impossible to quantify these two phases separately for the majority of the samples. Hence, we will treat the maghemite ($\gamma\text{-Fe}_2\text{O}_3$) and magnetite (Fe_3O_4) phase together as “spinel phase” in the following. It should be noted that there is evidence for conversion of Fe_3O_4 to $\gamma\text{-Fe}_2\text{O}_3$ during the annealing steps for all samples, manifested by a shift of the broadened peaks to higher angles, i.e., shift of the lattice constants to lower values (from ~ 8.40 to $\sim 8.34\text{ \AA}$), in combination with the occurrence of the aforementioned weak reflexes at 24° and 26° , respectively. This conversion

Fig. 2 Typical XRD pattern of samples A and B without heat treatment as synthesized and stored under ambient conditions for 7 weeks. Main reflexes are marked (asterisk symbol, spinel; degree sign, wustite; number sign, iron)



takes place in addition to the conversion of the material to $\alpha\text{-Fe}_2\text{O}_3$.

In the following, we focus on the thermally induced evolution of hematite ($\alpha\text{-Fe}_2\text{O}_3$), which is the most stable iron oxide phase.

The phase contents of freshly prepared sample A (diameter 40 ± 10 nm) are presented in Fig. 3b. The dominating phase is the wustite phase. Since there are no peaks at 24° or 26° , we conclude that the spinel phase content is dominated by maghemite. Crystallite size estimation based on XRD by the Scherrer method (Scherrer 1918) results in a smaller coherence volume for the spinel phase with values of around 8 nm, compared with an average crystallite size of 22 nm for the wustite phase for sample A. Based on the fact that in the TEM images no separated particles with diameter of 10 nm are observed, and based on the relative volume fraction of the phases, it can be concluded that the particles must be polycrystalline. However, in TEM images, only a few particles show a significant contrast difference indicating polycrystallinity.

Sample B shows an initial phase composition of almost equal amounts of wustite and the spinel phase (see Fig. 4), but, in contrast to sample A, a small amount of pure α -iron is present in the particles. We assume that this iron originates from disproportionation of wustite to magnetite and pure iron. This effect is well known for wustite bulk material when cooled down slowly to room temperature from temperatures above 567°C (Cornell and Schwertmann 2003). Due to the particle size, they may also show this property. There may be two reasons

why we could not observe elemental iron in sample A: first, due to the larger surface to volume ratio, iron formed during the cooling process under inert atmosphere would oxidize rapidly when the particles are exposed to atmosphere during the preparation for XRD. Second, small wustite particles appear to be stable against disproportionation, as observed by Chen et al. (2010), who observed a slow oxidation of such wustite particles prepared in a very similar way to the spinel phase within several months without disproportionation. The crystallite size of the iron is determined to 30 nm from the XRD measurement. Since we could not find isolated particles with this size on the TEM sample, we conclude that the iron must be part of the large particles.

The phase composition of the freshly prepared samples does not change rapidly under ambient conditions. The phase evolution of samples stored for 7 weeks under ambient conditions can be seen in Fig. 2. The phase contents of these samples are shown in Fig. 3b and Fig. 4b, respectively. Sample A shows an increase of the spinel phase content from 15 to 28%, while sample B shows only a change from 50 to 55% due to slow oxidation. There is no evidence of the formation of the hematite phase at room temperature.

Results II: annealing experiments

Evolution of the diffraction pattern for both batches during the annealing process is shown in Fig. 3a and Fig. 4a, respectively.

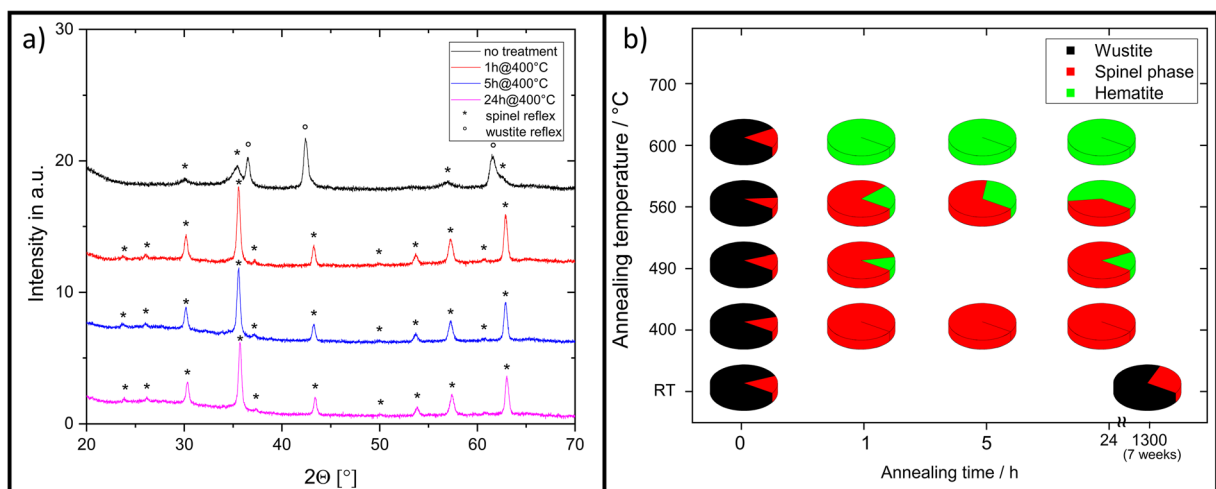


Fig. 3 a Typical XRD pattern of sample A after thermal treatment @400 °C. b Phase contents (by weight) of sample A for various thermal treatments

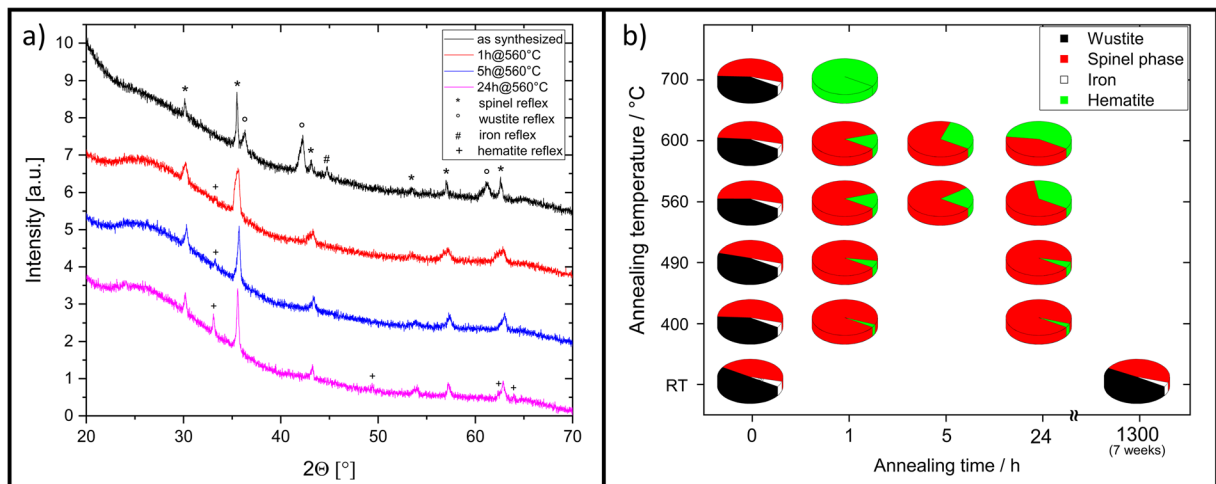


Fig. 4 **a** Typical XRD pattern of sample B after thermal treatment @ 560 °C. **b** Phase contents (by weight) of sample B for various thermal treatments

When annealed at 400 °C for 1 h, sample A shows a full conversion from wustite to the spinel phase (see Fig. 3). The spinel phase remains stable even for annealing times up to 24 h. This effect has also been observed for particles of 10 nm in size that were synthesized by the same method (Krispin et al. (2012)). The same annealing procedure applied to sample B leads to a small amount of hematite phase. It should be mentioned that the amount of hematite phase stays constant at least for annealing times up to 96 h (not shown). We note also that the amount of hematite phase in the annealed sample roughly corresponds to the amount of pure iron in the freshly prepared sample. To achieve a full conversion to hematite within 1 h, a minimum temperature of 600 °C is required in case of sample A and of 700 °C for sample B, respectively.

The crystallite sizes (as determined from XRD) of the spinel phase of sample B is plotted over the annealing time for an annealing temperature of 400 °C in Fig. 5. For other temperatures, similar behavior is observed. The crystallite size passes through a minimum at 1-h annealing time. After this minimum, it increases until it saturates after 48 h. This leads to the assumption that the particles develop from polycrystalline to nearly single-crystalline during the annealing procedure. The tendency to single-crystalline material is confirmed by the comparison of crystallite size determined by TEM and XRD, which agree very well. The lattice parameter of the spinel phase decreases during the annealing process from 8.38 to 8.35 Å as can be seen from Fig. 5b. In the first hour, a drastic drop of the lattice constant is

observed. After this, the value slowly decreases within the next 96 h, still not reaching the literature value for maghemite.

During the annealing process of sample B, a change of the particle shape from square-edged cubic to rounded-off shapes is observed as shown in Fig. 6a. At the same time, the weak structures visible in the TEM images of the particles apparently vanish suggesting a decrease of lattice defects and strain due to annealing.

Significant coagulation of the particles is observable at annealing temperatures above 600 °C for both samples. Figure 6b shows coagulated particles of sample A after 24 h at 600 °C. The initially well separated, 40 ± 10 -nm spherical particles have transformed to pure hematite particles with a non-uniform size of > 100 nm, aggregated to larger clusters. Interestingly, the average crystal size determined by XRD is still around 40 nm.

Discussion

The observed evolution of the iron oxide nanoparticle phases, i.e., from wustite to hematite, with intermediate meta-stable spinel-like phases magnetite and maghemite, is expected for nanoparticles heated at ambient conditions. However, the detailed temperature dependencies and transition rates are size-dependent and differ from those expected for bulk material.

Under ambient conditions, the phase composition of the large particles is stable, while the small particles show a slow oxidation, manifested in an increase of

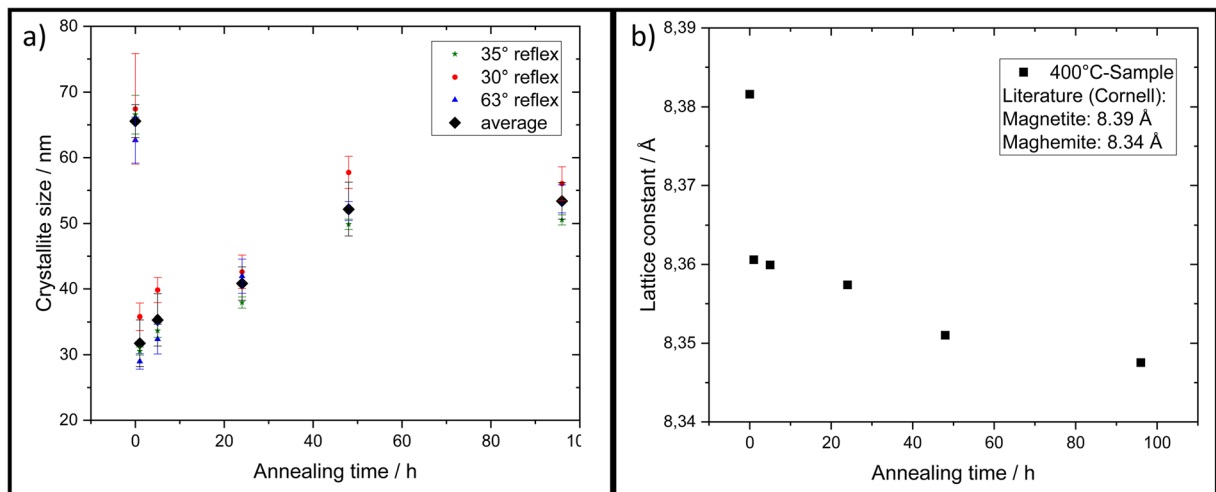


Fig. 5 a Crystallite sizes of the spinel phase from XRD of sample B (400 °C) after different annealing times with pronounced minimum after 1 h. Average value is determined from fitting the three most intense reflexes at $2\theta = n30^\circ$, 35° , and 63° , respectively. b

Lattice constant evolution from spinel phase, sample B (400 °C). Literature values for bulk maghemite and magnetite (Cornell and Schwertmann 2003) correspond to top and bottom border of diagram, respectively

the spinel phase from 16 to 28% (by weight) within 7 weeks. The higher reactivity of the smaller particles can be explained by their larger surface area in combination with shorter diffusion paths.

All annealed particles show in a first step a strong increase of the spinel phase. After this increase, the spinel phase fraction is constant for temperatures ≤ 490 °C for at least 24 h. During further annealing, the lattice constant of the spinel phase decreases, indicating an increasing amount of maghemite. The conversion rate slows down after the first hour. We assume that this can be explained by the fast oxidation of the surface of the particles within the first hour, followed by a slower oxidation of the core, based on diffusion.

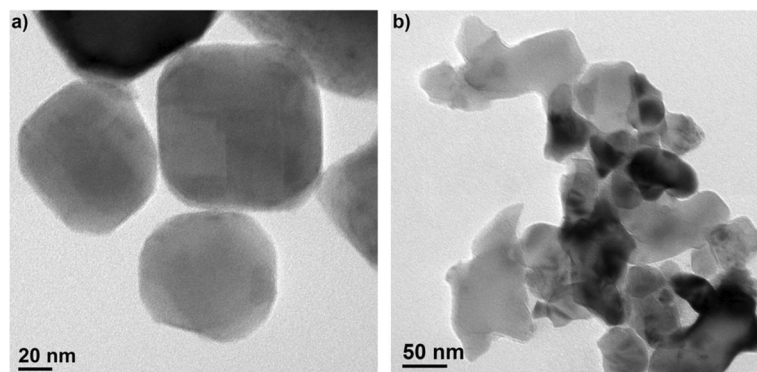
For higher temperatures, the spinel phase converts irreversibly to the hematite phase. The increase of the relative amount of the hematite phase is larger for

smaller particles (40 ± 10 nm) than for larger particles (95 ± 15 nm). From this observation, we conclude that the process is dominated by diffusion and that size effects (surface/volume energy ratio) do not play an important role.

The behavior of the smaller particles is consistent to literature for small γ - Fe_2O_3 particles around 12 nm. Here, Ye et al. (1998) found the onset of the transition from γ - Fe_2O_3 to α - Fe_2O_3 at around 470 °C. At the same time, the average crystallite size of the hematite phase is increasing with increasing temperature up to 54 nm at a quenching temperature of 730 °C, while the crystallite size of the γ - Fe_2O_3 phase is almost constant up to 470 °C. Furthermore, the transition temperature increases with decreasing grain size (Ye et al. 1998).

At first sight, this may also not match thermodynamic considerations, assuming that the most stable phase

Fig. 6 a Shape change of cubic particles after 94 h@400 °C; b coagulation of particles (sample A) after 24 h@600 °C



(based on the volume energy contribution) is hematite. One would expect that for smaller particles the energy barrier for the transformation from maghemite to hematite is higher, compared with large particles or bulk material. Here the opposite seems to be the case. However, the situation is more complex due to the fact that the particles are not single-crystalline. A closer inspection of the spinel phase of the larger particles reveals a drastic decrease of the crystallite sizes after 1 h calcination, yet below the size of the corresponding crystallites of the smaller particles. This may explain the lower transition temperature and its dependency on the crystallite sizes. The reason for this reduction of the crystallite sizes is not finally known. It could be explained by lattice strain caused by the volume change due to oxidation of the iron and wüstite phase in the large particles. However, other mechanisms like defect accumulation and ordering as proposed in Vasilevskaia et al. (2016) could be possible.

The crystallite size of the spinel phase increases slowly during further annealing and saturates after 48 h at around 50–60 nm for the large particles. The hematite crystal size, however, grows within the first 24 h of annealing up to 80 nm and stays constant for longer times. The hematite crystals in the small particles, however, do not show such a growing behavior. Once formed, for all temperatures and annealing times values of ~40 nm were found (not shown), even after the particles start to coagulate (Fig. 6b). The spinel phase in the small particles just grows during the first hour, saturating at around 30 nm (not shown).

Conclusion

The transition of wüstite/spinel nanoparticles to pure hematite particles was observed for different annealing temperatures and times. The minimum temperature for a full conversion within 1 h was 600 °C for 30–50-nm-sized particles, whereas larger particles of 80–110 nm required 700 °C. At lower temperatures, up to annealing times of 24 h, no full conversion to hematite was observed for both particle size distributions. Up to 400 °C, there seems to be no significant change of the spinel phase to hematite, but a slight change of the lattice constant is observed, indicating the conversion from magnetite to maghemite.

The crystallite sizes of the hematite and spinel phase shows a different behavior for the small and large

particles, respectively. In the large particles (80–110 nm), the crystallite size of the spinel phase decreases during the first annealing step, before it increases again up to 40–50 nm after 48 h. Further, the hematite crystallite sizes in the large particles grow until a value of 80 nm is reached after 24 h of annealing. The small particles (30–50 nm) do not show such a behavior. Instead, the crystallite sizes of the hematite phase, once formed, show an average value of 40 nm for all temperatures and times. The size of the spinel crystallites increases during the first hour from 8 nm to about 30 nm for all temperatures, remaining constant for longer annealing times.

Author contributions

AU: concept, phase analysis, TEM.

NR: sample preparation, XRD measurements.

SH: discussing scientific content.

Compliance with ethical standards

Conflict of interest The authors declare that they have no conflict of interest.

References

- Armijo LM, Brandt YI, Mathew D, Yadav S, Maestas S, Rivera AC, Cook NC, Withers NJ, Smolyakov GA, Adolphi NL, Monson TC, Huber DL, Smyth HDC, Osiński M (2012) Iron oxide nanocrystals for magnetic hyperthermia applications. *Nanomaterials* 2:134–146
- Bean CP, Livingston JD (1959) Superparamagnetism. *J Appl Phys* 30(4):120S–129S
- Berkowitz AE, Schuele WJ, Flanders PF (1968) Influence of crystallite size on the magnetic properties of acicular γ -Fe₂O₃ particles. *J Appl Phys* 39:1261–1263
- Chen CJ, Chiang RK, Lai HY, Lin CR (2010) Characterization of monodisperse wüstite nanoparticles following partial oxidation. *J Phys Chem C* 114:4258–4263
- Cornell RM, Schwertmann U (2003) The iron oxides: "structure, properties, reactions, occurrence and uses", 2nd edn. VCH, Weinheim
- Dutz S, Hergt R (2013) Magnetic nanoparticle heating and heat transfer on a microscale: basic principles, realities and physical limitations of hyperthermia for tumour therapy. *Int J Hypertherm* 29(8):790–780
- Fang C, Zhang M (2009) Multifunctional magnetic nanoparticles for medical imaging applications. *J Mat Chem* 19:6258–6266
- Huang WC, Lyu LM, Yang YC, Huang MH (2012) Synthesis of Cu₂O nanocrystals from cubic to rhombic dodecahedral structures and their comparative photocatalytic activity. *J Am Chem Soc* 134:1261–1267

- Janzen C, Knipping J, Rellinghaus B, Roth P (2003) Formation of silica-embedded iron-oxide nanoparticles in low-pressure flames. *J Nanopart Res* 5:589–596
- Kovalenko MV, Bodnarchuk MI, Lechner RT, Hesser G, Schäffler F, Heiss W (2007) Fatty acid salts as stabilizers in size- and shape-controlled nanocrystal synthesis. *J Am Chem Soc* 129:6352–6353
- Krispin M, Ullrich A, Horn S (2012) Crystal structure of iron-oxide nanoparticles synthesized from ferritin. *J Nanopart Res* 14:669–680
- Li P, Miser DE, Rabiei S, Yadav RT, Hajaligol MR (2003) The removal of carbon monoxide by iron oxide nanoparticles. *Applied Catalysis B* 43:151–162
- Li S, Jiang ZH, Jiang Q (2008) Thermodynamic phase stability of three nano-oxides. *Mater Res Bull* 43:3149–3154
- Liang S, Teng F, Bulgan G, Zong R, Zhu Y (2008) Effect of phase structure of MnO₂ nanorod catalyst on the activity for CO oxidation. *J Phys Chem C* 112:5307–5315
- Mendili YE, Bardeau JF, Randrianantoandro N, Grasset F, Grenèche JM (2012) Insights into the mechanism related to the phase transition from γ -Fe₂O₃ to α -Fe₂O₃ nanoparticles induced by thermal treatment and laser irradiation. *J Phys Chem C* 116:23785–23792
- Park J, An K, Hwang Y, Park JG, Noh HJ, Kim JY, Park JH, Hwang NM, Hyeon T (2004) Ultra-large-scale syntheses of monodisperse nanocrystals. *Nat Mater* 3:891–895
- Poizot P, Laruelle S, Grugeon S, Dupont L, Tarascon JM (2000) Nano-sized transition-metal oxides as negative-electrode materials for lithium-ion batteries. *Nature* 407:496–499
- Scherrer P (1918) Bestimmung der Größe und der inneren Struktur von Kolloidteilchen mittels Röntgenstrahlen. *Göttinger Nachrichten* 2:98–100
- Shavel A, Liz-Marzán LM (2009) Shape control of iron oxide nanoparticles. *Phys Chem Chem Phys* 11:3762–3766
- Vasilevskaia AK, Popkov VI, Valeeva AA, Rempel AA (2016) Formation of nonstoichiometric titanium oxides nanoparticles Ti_nO_{2n-1} upon heat-treatments of titanium hydroxide and anatase nanoparticles in a hydrogen flow. *Russ J Appl Chem* 89:1211–1220
- Wetterskog E, Agthe M, Mayence A, Grins J, Wang D, Rana S, Ahniyaz A, Salazar-Alvarez G, Bergström L (2014) Precise control over shape and size of iron oxide nanocrystals suitable for assembly into ordered particle arrays. *Sci Technol Adv Mater* 15:055010
- Yavuz CT, Mayo JT, Suchecki C, Wang J, Ellsworth AZ, D’Couto H, Quevedo E, Prakash A, Gonzalez L, Nguyen C, Kelty C, Colvin VL (2010) Pollution magnet: nano-magnetite for arsenic removal from drinking water. *Environ Geochem Health* 32:327–334
- Ye X, Lin D, Jiao Z, Zhang L (1998) The thermal stability of nanocrystalline maghemite Fe₂O₃. *J Phys D Appl Phys* 31:2739–2744

Publisher's note Springer Nature remains neutral with regard to jurisdictional claims in published maps and institutional affiliations.